

# Pediatric radiation dosimetry for positron-emitting radionuclides using anthropomorphic phantoms

Tianwu Xie

*Division of Nuclear Medicine and Molecular Imaging, Geneva University Hospital, CH-1211 Geneva 4, Switzerland*

Wesley E. Bolch

*Departments of Biomedical Engineering, University of Florida, Gainesville, Florida 32611*

Choonsik Lee

*Division of Cancer Epidemiology and Genetics, National Cancer Institute, National Institute of Health, Rockville, Maryland 20850*

Habib Zaidi<sup>a)</sup>

*Division of Nuclear Medicine and Molecular Imaging, Geneva University Hospital, CH-1211 Geneva 4, Switzerland; Geneva Neuroscience Center, Geneva University, CH-1205 Geneva, Switzerland; and Department of Nuclear Medicine and Molecular Imaging, University of Groningen, University Medical Center Groningen, 9700 RB Groningen, The Netherlands*

(Received 26 June 2013; revised 25 July 2013; accepted for publication 12 August 2013; published 5 September 2013)

**Purpose:** Positron emission tomography (PET) plays an important role in the diagnosis, staging, treatment, and surveillance of clinically localized diseases. Combined PET/CT imaging exhibits significantly higher sensitivity, specificity, and accuracy than conventional imaging when it comes to detecting malignant tumors in children. However, the radiation dose from positron-emitting radionuclide to the pediatric population is a matter of concern since children are at a particularly high risk when exposed to ionizing radiation.

**Methods:** The authors evaluate the absorbed fractions and specific absorbed fractions (SAFs) of monoenergy photons/electrons as well as *S*-values of 9 positron-emitting radionuclides (C-11, N-13, O-15, F-18, Cu-64, Ga-68, Rb-82, Y-86, and I-124) in 48 source regions for 10 anthropomorphic pediatric hybrid models, including the reference newborn, 1-, 5-, 10-, and 15-yr-old male and female models, using the Monte Carlo N-Particle eXtended general purpose Monte Carlo transport code.

**Results:** The self-absorbed SAFs and *S*-values for most organs were inversely related to the age and body weight, whereas the cross-dose terms presented less correlation with body weight. For most source/target organ pairs, Rb-82 and Y-86 produce the highest self-absorbed and cross-absorbed *S*-values, respectively, while Cu-64 produces the lowest *S*-values because of the low-energy and high-frequency of electron emissions. Most of the total self-absorbed *S*-values are contributed from non-penetrating particles (electrons and positrons), which have a linear relationship with body weight. The dependence of self-absorbed *S*-values of the two annihilation photons varies to the reciprocal of 0.76 power of the mass, whereas the self-absorbed *S*-values of positrons vary according to the reciprocal mass.

**Conclusions:** The produced *S*-values for common positron-emitting radionuclides can be exploited for the assessment of radiation dose delivered to the pediatric population from various PET radiotracers used in clinical and research settings. The mass scaling method for positron-emitters can be used to derive patient-specific *S*-values from data of reference phantoms. © 2013 American Association of Physicists in Medicine. [<http://dx.doi.org/10.1118/1.4819939>]

Key words: radiation dosimetry, PET, Monte Carlo, computational models, pediatrics

## 1. INTRODUCTION

Positron emission tomography (PET) is nowadays considered as a key molecular imaging technique playing a pivotal role in clinical diagnosis, staging, monitoring of therapeutic response, and surveillance of clinically localized diseases in patients.<sup>1</sup> For the pediatric population, recent reports seem to indicate that hybrid PET/CT imaging exhibits significantly higher sensitivity, specificity, and accuracy compared to conventional imaging in evaluating pedi-

atric malignancies.<sup>2-4</sup> In this regard, improved dose regimens and dedicated low dose pediatric whole-body PET/CT protocols have been devised.<sup>5,6</sup> Yet, the radiation absorbed dose delivered to pediatric patients from standalone or hybrid nuclear medical imaging examinations is still a matter of concern.<sup>7-9</sup>

With the same absolute level of radiation dose, children may experience greater deterministic effects from ionizing radiation than adults, because they have a proportionally higher percentage of replicating cells, which are more radiosensitive than other cells.<sup>10</sup> The stochastic effects (e.g., cancer and

hereditary effects) are mainly caused by radiation-induced DNA mutation or symmetrical translocations in cells, and follow a positive linear no-threshold dependence on the absorbed radiation dose.<sup>11,12</sup> The latent period of stochastic effects can vary from 2 to 30 yr.<sup>13,14</sup> Children have higher stochastic risks from ionizing radiation compared to adults and pediatric patients have longer postirradiation life period for the deleterious effects of radiation to become apparent. In this context, the accurate assessment of radiation dose delivered to the pediatric population involving the use of standalone or hybrid diagnostic imaging techniques (e.g., PET, PET-CT) can help in making an effective usage of various combinations of PET tracers and optimize the radiation protection of pediatric patients.

To this end, various computational models have been developed to simulate the morphology and internal anatomic structures of children at different ages and are used to assess the radiation dose delivered to pediatric patients during x-ray CT and nuclear medical imaging procedures.<sup>15</sup> In 1960, Snyder and Fisher developed the first series of stylized pediatric and adult anatomical models, which employ mathematical equations (e.g., planes, cylinder, cone, ellipsoid, or spheroid) to represent body organs and tissues for use in radiation dosimetry calculations.<sup>16</sup> Subsequently, a number of improved human models were derived,<sup>15,17–19</sup> some of which were published as series of Medical Internal Radiation Dose (MIRD) pamphlets.<sup>20–22</sup> The successive stylized models are known as “MIRD-type phantoms.” Stabin *et al.* produced a series of widely used personal computer software codes (MIRDose and OLINDA/EXM) for human internal dosimetry calculations based on the MIRD schema and mathematical computational models.<sup>23,24</sup> About 30 yr ago, the emergence of tomographic medical imaging modalities stimulated the development of realistic voxel-based anatomical models, currently adopted as a standard in radiation dosimetry calculations. Pioneered by Williams *et al.*<sup>25</sup> and Zankl *et al.*,<sup>26</sup> voxel-based pediatric models were constructed based on CT images of children. Since then, a variety of voxel-based pediatric models covering various ages were developed by different investigators. Petoussi-Hens *et al.*<sup>27</sup> developed the GSF family of phantoms including 8-week-old baby and 7-yr-old child. Christ *et al.*<sup>28</sup> constructed the virtual family models including the 6-yr-old male and 7-yr-old female. Nagaoka *et al.*<sup>29</sup> developed 3-, 5-, and 7-yr-old Japanese children models, whereas Li *et al.*<sup>30</sup> developed two pediatric phantoms based on a 5-week-old girl and a 12-yr-old boy. Nipper *et al.*<sup>31</sup> and Lee *et al.*<sup>32,33</sup> of the University of Florida elaborated a series of pediatric voxel models of various ages. Recently introduced hybrid models employ nonuniform rational B-splines (NURBS) or polygon mesh surfaces to represent the surface contours of organs and tissues, standing for an important step in computational phantom development.<sup>34</sup> Based on organ and tissue masses data reported in the ICRP 89,<sup>35</sup> Lee *et al.*<sup>36,37</sup> constructed the first reference hybrid pediatric models (referred to as UF-NCI phantoms), including the reference newborn, 1-, 5-, 10-, and 15-yr-old male and female models, for computational radiation dosimetry. Lima *et al.*<sup>38</sup> developed 5- and 10-yr-old pediatric models based on poly-

gon mesh surfaces, whereas Stabin *et al.*<sup>39</sup> developed series of reference adult, children, and pregnant female for radiation dosimetry.

In most studies reported in the literature,<sup>7,40</sup> the estimation of cumulative radiation dose from PET tracers to children was performed using dosimetric parameters of positron-emitters and mathematical pediatric phantoms specified in ICRP publications,<sup>41–43</sup> MIRDose,<sup>23</sup> or OLINDA<sup>24</sup> packages. However, significant differences have been reported between dosimetric results of stylized and voxel-based models of the same subject.<sup>44–47</sup> Therefore, the assessment of radiation dose for commonly used positron-emitting radionuclides in new generation anthropomorphic pediatric phantoms is highly desired.

In this work, we use the University of Florida-National Cancer Institute (UF-NCI) family of pediatric models to perform Monte Carlo-based particle transport simulations of monoenergy photons/electrons and spectra corresponding to decay schemes of commonly used positron-emitting radionuclides (C-11, N-13, O-15, F-18, Cu-64, Ga-68, Rb-82, Y-86, and I-124) to calculate the absorbed fractions (AFs), specific absorbed fractions (SAFs), and *S*-values for the considered series of anatomical models. The obtained radiation dosimetry database can be used for the assessment of radiation dose to children undergoing PET imaging procedures at different ages. Understanding the variability of the absorbed dose with body weight is important to appreciate the uncertainties involved in internal radiation dosimetry calculations.

## 2. MATERIALS AND METHODS

### 2.A. Computational reference pediatric phantoms

The UF-NCI phantom series, including the reference newborn, 1-, 5-, 10-, and 15-yr-old male and female models, were used in this work to represent reference children for Monte Carlo-based internal radiation dosimetry calculations. Voxel-based models were generated from original hybrid surface-represented UF-NCI models. A united voxel dimension of  $1.8 \times 1.8 \times 3 \text{ mm}^3$  was set for all voxelized pediatric models to minimize the difference across different models. The cartilage, cortical bone, and spongiosa at different bone sites (e.g., skull, ribs, and femurs) were combined. The spongiosa was treated as a mixture of active marrow, inactive marrow, and trabecular bone according to the reported mass of these suborgans in reference children.<sup>33</sup> The calculated mass proportions of these suborgans in the spongiosa are listed in Table I. The homogeneous organs, such as the left lung and the right lung, the submaxillary salivary gland, and the sublingual salivary gland, were merged as one identified region. The blood vessel in the phantom refers to the blood in the arteries and the veins. These actions were taken for the sake of convenience to calculate the effective dose in the pediatric population.<sup>48</sup> A total of 50 organs and tissues were identified in pediatric phantoms. Figure 1 shows the front 3D views of the 10 pediatric phantoms used in this work. The number of voxels in each organ of the pediatric phantoms was calculated and multiplied by the voxel volume and the corresponding age-dependent

TABLE I. Calculated mass proportions of active marrow, inactive marrow, and trabecular bone in the spongiosa of reference children.

Tissues	Newborn (%)	1-yr (%)	5-yr (%)	10-yr (%)	15-yr (Male) (%)	15-yr (Female) (%)
Active marrow	54.1	47.2	41.7	34.3	30.2	30.3
Inactive marrow	-	6.3	19.6	34.3	41.4	41.8
Trebacular bone	45.9	46.5	38.7	31.3	28.3	28.0

tissue density<sup>35</sup> to yield the organ mass. Table II summarizes the body weight and the calculated mass for each organ of the voxel-based computational pediatric phantoms.

## 2.B. Monte Carlo simulations

The Monte Carlo N-Particle eXtended (MCNPX) code (version 2.5.c) was chosen for radiation transport simulation.<sup>49</sup> Uniformly distributed photon and electron sources, using 20 discrete photon energies ranging from 0.01 to 3.0 MeV and 13 selected electron energies ranging from

0.1 to 3.0 MeV, and nine positron-emitting sources (C-11, N-13, O-15, F-18, Cu-64, Ga-68, Rb-82, Y-86, and I-124) were simulated in 50 source regions. The decay data of the investigated positron-emitting radionuclides were obtained from the Health Physics Society electronic resource.<sup>50</sup> The energy deposited by photons, electrons, and positrons in the target regions were recorded in unit of MeV per particle using the MCNPX tally card \*F8. A specific F6 tally card was used to record the energy deposited by the two 511 keV photons resulting from electron-positron annihilation in unit of MeV/g per particle. An in-house C++ code was developed to extract the numbers from the MCNPX output files, and the results of F6 tally were multiplied by the target mass to transform the unit to MeV per particle. The density and elemental composition of organs/tissues for each anatomical model were obtained from the reported reference pediatric data of ICRP Report 89.<sup>35</sup> A total of  $6.0 \times 10^6$  primary particle histories (NPS) were generated such that the statistical uncertainty in terms of coefficient of variation (COV) was less than 3% in most cases. Ten parallel MCNPX simulation processes were performed on a 12-core workstation with 2.4 GHz Intel Xeon processors and 32 GB random access memory (RAM) running under Microsoft Windows 7 operating system.

## 2.C. Dosimetry calculations

The AF and SAF are the basic measures of internal radiation dose. The former describes the proportion of energy deposited in the target organ released in source organs, whereas the latter is defined as the ratio of the AF and the target mass, which reflects the mean AF in the target region and as such, is more informative and comprehensive than the AF. These measures are used in the calculation of individual organ absorbed doses, organ equivalent doses, and the whole-body effective dose. In the MIRD formalism, the radiation absorbed dose delivered to any target tissue  $r_T$  from source organ  $r_S$  is given by Eqs. (1) and (2):<sup>51</sup>

$$\begin{aligned}
 D(r_T, T_D) &= \sum_{r_S} \int_0^{T_D} A(r_S, t) S(r_T \leftarrow r_S) dt \\
 &= \sum_{r_S} \tilde{A}(r_S, T_D) S(r_T \leftarrow r_S), \tag{1}
 \end{aligned}$$

$$\begin{aligned}
 S(r_T \leftarrow r_S) &= \frac{1}{M(r_T)} \sum_i E_i Y_i \phi(r_T \leftarrow r_S, E_i) \\
 &= \sum_i E_i Y_i \Phi(r_T \leftarrow r_S, E_i), \tag{2}
 \end{aligned}$$

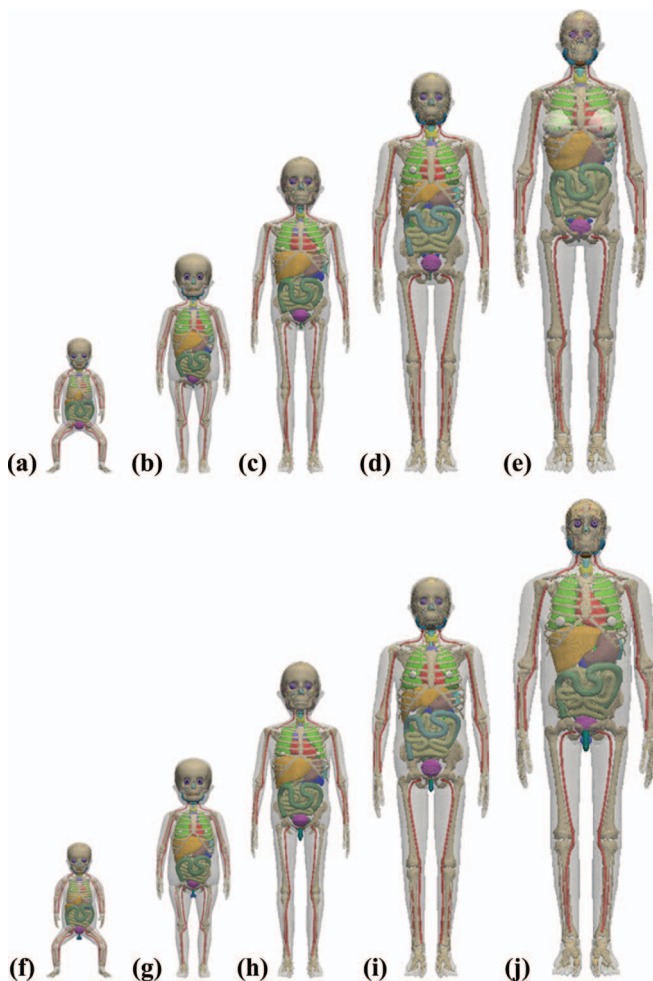


FIG. 1. 3D visualization of computational pediatric phantoms showing: (a) the newborn female phantom, (b) the 1-yr female phantom, (c) the 5-yr female phantom, (d) the 10-yr female phantom, (e) the 15-yr female phantom, (f) the newborn male phantom, (g) the 1-yr male phantom, (h) the 5-yr male phantom, (i) the 10-yr male phantom, and (j) the 15-yr male phantom.

TABLE II. Organ masses and total body weights of the 10 paediatric phantoms used in this work.

Organ mass (g)	Newborn		1-yr		5-yr		10-yr		15-yr	
	Female	Male	Female	Male	Female	Male	Female	Male	Female	Male
Adipose tissue	658.7	659.3	3653.0	3652.6	4642.8	4649.0	6435.8	6435.8	11649.8	6748.7
Adrenal	5.9	5.9	4.0	4.0	5.0	5.0	7.0	7.0	9.0	10.0
Brain	314.8	314.8	945.2	945.2	1241.0	1241.0	1305.4	1305.4	1294.0	1415.5
Colon	60.6	60.6	100.2	100.2	208.1	208.1	300.5	300.4	454.4	541.5
Colon Wall	16.8	16.8	49.4	49.4	118.4	118.4	206.9	206.8	295.6	297.8
Colon Content	43.8	43.8	50.8	50.8	89.7	89.7	93.6	93.6	158.8	243.7
Gall Bladder	3.3	3.3	9.4	9.4	17.5	17.5	30.2	30.2	48.7	52.2
Gall Bladder Wall	0.5	0.5	1.4	1.4	2.6	2.6	4.4	4.4	7.2	7.5
Gall Bladder Content	2.8	2.8	8.0	8.0	14.9	14.9	25.8	25.8	41.5	44.7
Heart	25.9	25.9	97.4	97.4	218.8	218.8	366.6	366.6	537.3	655.1
Heart Wall	19.9	19.9	50.0	50.0	85.2	85.2	138.3	138.3	219.7	229.9
Heart Content	6.0	6.0	47.4	47.4	133.6	133.6	228.3	228.3	317.6	425.2
Kidney	26.0	26.0	72.7	72.7	113.8	113.8	187.2	187.2	250.4	261.1
Kidney Cortex	18.3	18.3	51.0	51.0	79.4	79.4	131.3	131.3	176.2	183.2
Kidney Medulla	6.5	6.5	18.2	18.2	28.8	28.8	46.8	46.8	62.1	65.2
Kidney Pelvis	1.3	1.3	3.5	3.5	5.6	5.6	9.1	9.1	12.0	12.8
Liver	128.6	128.6	327.1	327.1	567.0	567.0	824.5	824.5	1290.5	1290.4
Lung	58.8	58.8	149.3	149.3	297.9	297.9	489.1	489.1	752.9	886.8
Pancreas	6.0	6.0	19.8	19.8	34.6	34.6	59.7	59.7	99.2	109.1
Salivary Glands	5.9	5.9	23.7	23.7	33.6	33.6	43.9	43.9	62.7	67.0
Small Intestine (SI)	60.7	60.7	131.0	131.0	249.2	249.2	518.2	519.1	775.5	770.6
SI Wall	29.3	29.3	82.1	82.1	210.9	210.9	355.6	357.5	496.4	503.3
SI Content	31.4	31.4	48.9	48.9	38.3	38.3	162.6	161.6	279.1	267.3
Spinal Cord	6.4	6.4	24.6	24.6	31.4	31.4	68.5	68.5	68.4	42.5
Spleen	9.4	9.4	28.7	28.7	49.6	49.6	79.4	79.4	128.9	128.7
Stomach	31.9	31.9	85.8	85.8	132.2	132.2	200.0	200.0	317.9	317.3
Stomach Wall	6.9	6.9	19.7	19.7	49.5	49.5	83.7	83.7	118.5	117.5
Stomach Content	25.0	25.0	66.1	66.1	82.7	82.7	116.3	116.3	199.4	199.8
Thymus	12.8	12.8	16.1	16.1	30.0	30.0	37.5	37.5	29.9	34.6
Thyroid	1.3	1.3	1.8	1.8	3.4	3.4	7.8	7.8	12.1	11.9
Urinary Bladder	13.8	13.8	18.7	19.8	76.4	76.3	121.7	121.8	166.5	190.4
Urinary Bladder Wall	3.9	3.9	8.8	8.9	15.7	15.6	24.3	24.8	34.3	39.4
Urinary Bladder Content	9.9	9.9	9.9	10.9	60.7	60.7	97.4	97.0	132.2	151.0
Blood Vessel	11.0	11.0	23.6	23.6	62.3	62.3	134.0	134.0	226.1	252.5
Muscle	1530.0	1532.8	3186.8	3155.3	7367.7	7364.3	16285.3	16288.4	26141.4	34689.0
Cortical Bone	76.4	76.4	293.3	293.3	735.7	735.7	1704.6	1704.6	2932.7	3264.6
Spongiosa	171.2	171.2	572.8	572.8	1266.7	1266.7	2668.8	2668.8	4047.8	4674.5
Testes	0.0	0.8	0.0	1.5	0.0	1.7	0.0	2.0	0.0	15.8
Ovaries	0.3	0.0	0.8	0.0	2.0	0.0	3.4	0.0	5.8	0.0
Prostate	0.0	0.8	0.0	1.0	0.0	1.2	0.0	1.6	0.0	4.3
Uterus	3.9	0.0	1.5	0.0	3.0	0.0	4.0	0.0	29.6	0.0
Cartilage	126.1	126.1	37.7	37.7	55.9	55.9	128.2	128.2	150.7	138.8
Penis	0.0	0.6	0.0	3.6	0.0	6.5	0.0	6.6	0.0	29.2
Pituitary Gland	0.1	0.1	0.2	0.2	0.3	0.3	0.4	0.4	0.5	0.5
Tonsil	0.1	0.1	0.5	0.5	2.0	2.0	2.9	2.9	2.9	2.9
Breast	0.1	0.1	0.4	0.4	0.9	0.9	7.6	7.6	306.7	14.7
Esophagus	2.0	2.0	4.9	4.9	9.9	9.9	17.8	17.8	27.9	29.4
Bronchi	0.4	0.4	2.0	2.0	3.0	3.0	3.6	3.5	7.3	8.0
Eye Balls	5.9	5.9	6.8	6.8	10.8	10.8	11.7	11.7	13.0	12.9
Larynx	1.3	1.3	3.9	3.9	6.8	6.8	11.8	11.8	14.4	21.7
Lens	0.1	0.1	0.2	0.2	0.3	0.3	0.4	0.4	0.4	0.5
Nasal Layer	0.8	0.8	2.1	2.1	8.5	8.5	9.0	9.0	9.0	11.5
Oral Cavity Layer	0.7	0.7	0.6	0.6	1.2	1.2	1.1	1.1	8.0	5.2
Pharynx	0.3	0.3	0.8	0.8	1.9	1.9	1.9	1.9	3.1	2.9
Tongue	3.5	3.5	9.8	9.8	18.8	18.8	31.5	31.5	52.8	55.4
Trachea	0.5	0.5	1.5	1.5	2.4	2.4	4.4	4.4	5.4	7.5
Skin	96.5	98.2	188.0	211.8	638.2	642.8	806.4	809.7	1690.1	1806.7
Total (kg)	3.5	3.5	10.0	10.0	18.2	18.2	32.9	32.9	53.6	58.6

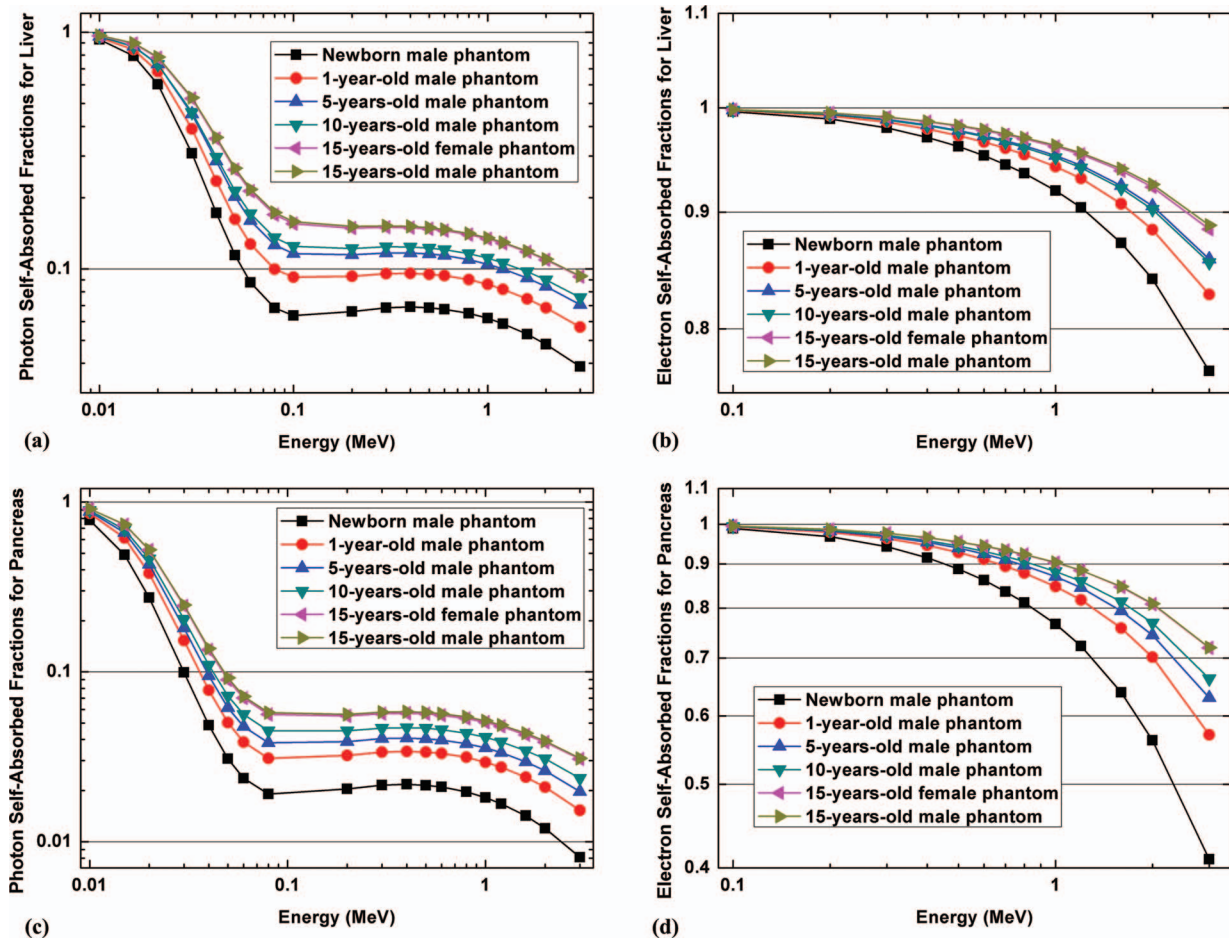


FIG. 2. Photon (a) and (c) and electron (b) and (d) self-absorbed fractions of the liver (a) and (b) and pancreas (c) and (d) for various pediatric models.

where  $\tilde{A}(r_S, T_D)$  is the cumulated (time-integrated) activity in the source organ over the dose-integration period  $T_D$ ,  $S(r_T \leftarrow r_S)$  is the  $S$ -value describing the equivalent dose rate in the target organ per unit activity in the source organ,  $E_i$  is the individual energy of the  $i$ th radiation,  $Y_i$  is the yield of  $i$ th radiation per nuclear transformation,  $M(r_T)$  is the mass of the target tissue,  $\Phi(r_T \leftarrow r_S, E_i)$  is the SAF, and  $\phi(r_T \leftarrow r_S, E_i)$  is the AF given by

$$\phi(r_T \leftarrow r_S, E_i) = \frac{E_d}{E_i}, \quad (3)$$

where  $E_d$  is the energy deposited in the target tissue. When the target organ becomes the source organ, the AF is also termed the self-AF.

For total body irradiating other organs, when uniform sampling probability is set to all body voxels, the absorbed fraction of the  $i$ th radiation in the target region is given by

$$\phi(r_T \leftarrow TB, E_i) = \frac{1}{E_i} \sum_{r_S} \omega(r_S) E_d(r_S), \quad (4)$$

where  $E_d(r_S)$  refers to the deposited energy in target tissue of the radiation emitted from source organ  $r_S$  and  $\omega(r_S)$  is the sampling probability in the source organ, which equals the volume proportion of the source organ in the total body.

Based on Eqs. (2) and (3), the  $S$ -value can be written as

$$S(r_T \leftarrow r_S) = \frac{E_d}{M(r_T)} \sum_i Y_i. \quad (5)$$

Equation (5) can be used to calculate the  $S$ -value of positron-emitters for different source-target pairs when the energy spectrum of emitted radiation is defined in the source description in Monte Carlo simulation.

### 3. RESULTS

#### 3.A. AFs and SAFs

The AFs and SAFs for monoenergetic photons and electrons for 50 source organs irradiating all targets, and  $S$ -values of the nine positron-emitting radionuclides for the considered source-target organ pairs were calculated in the considered pediatric phantoms. Figure 2 shows photon and electron self-AFs for the liver and the pancreas for the newborn, 1-, 5-, 10-yr-old male, and 15-yr-old male and female phantoms. Traditionally, the electron self-absorbed organ SAFs for human internal radiation dosimetry are assumed to be equal to 1, whereas the energy deposited from cross-irradiating electrons is commonly neglected.<sup>52</sup> The results shown in Figs. 2(b) and 2(d) deviate from this assumption at higher electron energies, particularly in organs of the smaller (e.g., newborn) phantom.

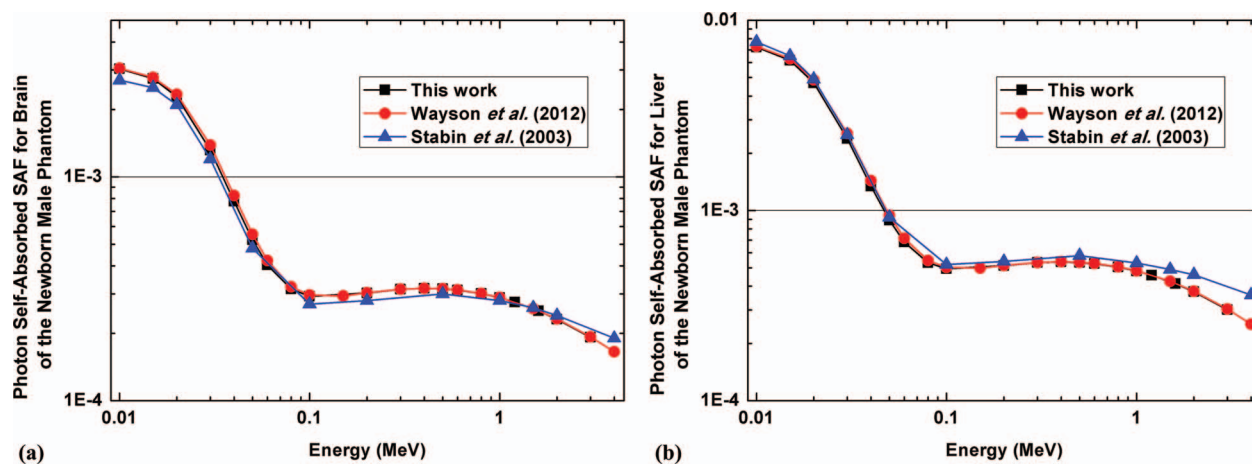


FIG. 3. Comparisons of photon self-absorbed SAFs for (a) the brain and (b) the liver of the newborn male phantom between this work, Wayson *et al.* (Ref. 46) and Stabin and Siegel (Ref. 53).

This can be explained by the fact that the increased source energy facilitates the escape of electrons and secondary particles from the source organ, while the smaller volume shortens the distance of particle transport and causes less energy deposition in the source region.

Comparisons between the results obtained in this work and those reported by Wayson *et al.*<sup>46</sup> and Stabin and Siegel<sup>53</sup> for photon self-absorbed SAF of the brain and liver in the newborn male phantom are illustrated in Fig. 3. A good agreement between our results and those reported in the literature can be observed, thus validating our simulation setup.

Small differences between the SAFs of the voxel-based pediatric phantoms used both in the current work and the study reported by Wayson *et al.*<sup>46</sup>, and the MIRD-type phantom used by Stabin and Siegel<sup>53</sup> can be observed. Differences of  $-0.15\%$  and  $5.32\%$  for brain SAFs were observed at a photon energy of 0.5 MeV between results obtained in this work and those reported by Wayson *et al.* and Stabin *et al.*, respectively.

Figure 4 shows photon and electron self-absorbed SAFs for the heart wall and liver of the representative pediatric phantoms. As can be seen in Fig. 4(c), the liver self-absorbed

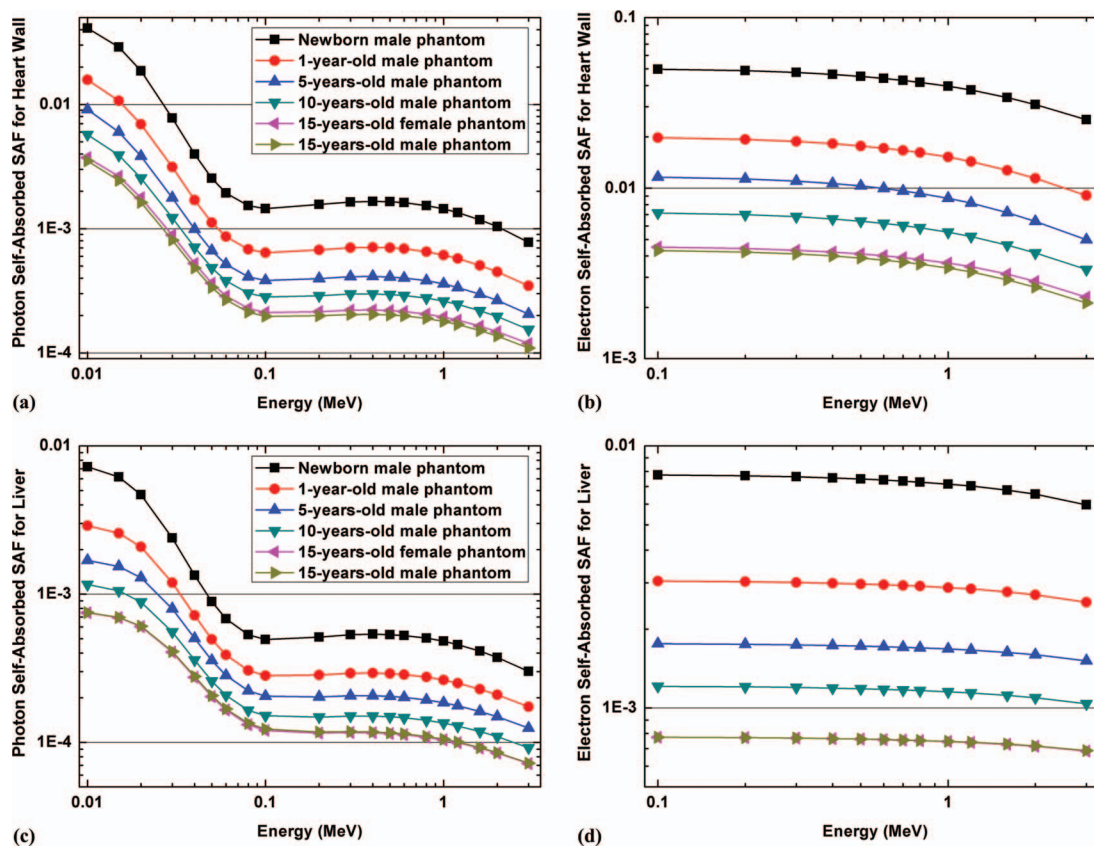


FIG. 4. Photon (a) and (c) and electron (b) and (d) self-absorbed fractions of the heart wall (a) and (b) and liver (c) and (d) for various pediatric models.

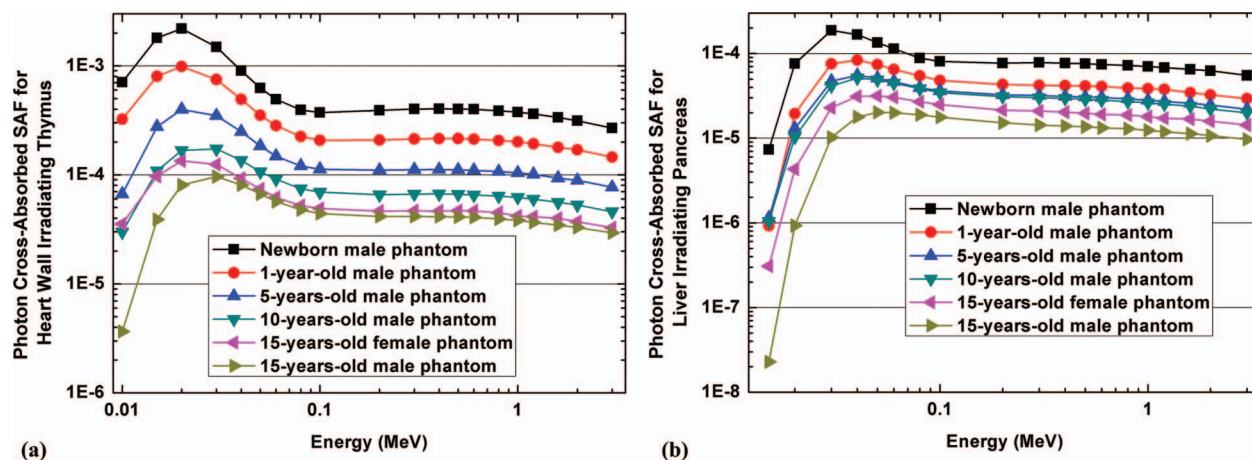


FIG. 5. Cross-absorbed photon SAFs for (a) the heart wall irradiating the thymus and (b) the liver irradiating the pancreas for various pediatric phantoms.

photon SAFs are 296%–864% higher in the newborn phantom and 66%–126% higher in the 5-yr-old phantom compared to the 15-yr-old male. Conversely, the liver self-absorbed electron SAFs are about 860% higher in the newborn phantom and 124% higher in the 5-yr-old phantom than in the 15-yr-old male model [Fig. 4(d)]. The self-absorbed SAFs at low energies are close to (organ mass)<sup>-1</sup>.

Figure 5 shows the cross-absorbed photon SAFs for the heart wall irradiating the thymus and the liver irradiating the pancreas. The photon cross-absorbed SAFs start initially with a speedy raise phase followed by gradual drop with increasing photon energy, peaking at around 30 keV. Owing to the smaller body size of children, the radiation exposure from cross-irradiation in young patients would be more significant in PET scanning.

**3.B. S-values**

Figure 6 shows the ratios of self-absorbed S-values of C-11 and O-15 between the results obtained in this work as well

as Stabin and Siegel<sup>53</sup> and those reported by Wayson *et al.*<sup>46</sup> for representative organs of the male newborn. For solid organs, there is good agreement between S-values of self-irradiation scenarios between this work and Wayson *et al.*<sup>46</sup> while for hollow organs, the self-absorbed S-values of organ walls are about 4%–8% larger than those of Wayson *et al.*<sup>46</sup> and present a higher sensitivity to changes in image resolution and corresponding voxel size (0.663 × 0.663 × 0.663 mm<sup>3</sup> for the model used by Wayson *et al.* and 1.8 × 1.8 × 3 mm<sup>3</sup> for the model used in this work), which cause differences between tissue contours. The ratios of S-value between Stabin and Siegel<sup>53</sup> and Wayson *et al.*<sup>46</sup> vary between 0.21 and 2.32, which may be attributed to the differences between the geometries of the stylized and voxel-based model.

Figures 7 and 8 illustrate self-absorbed S-values for the kidney, liver, lung, and salivary gland and cross-absorbed S-values of different source-target organ pairs for the defined pediatric phantoms and the 9 considered positron-emitting radionuclides. For all radionuclides, the self-absorbed S-values

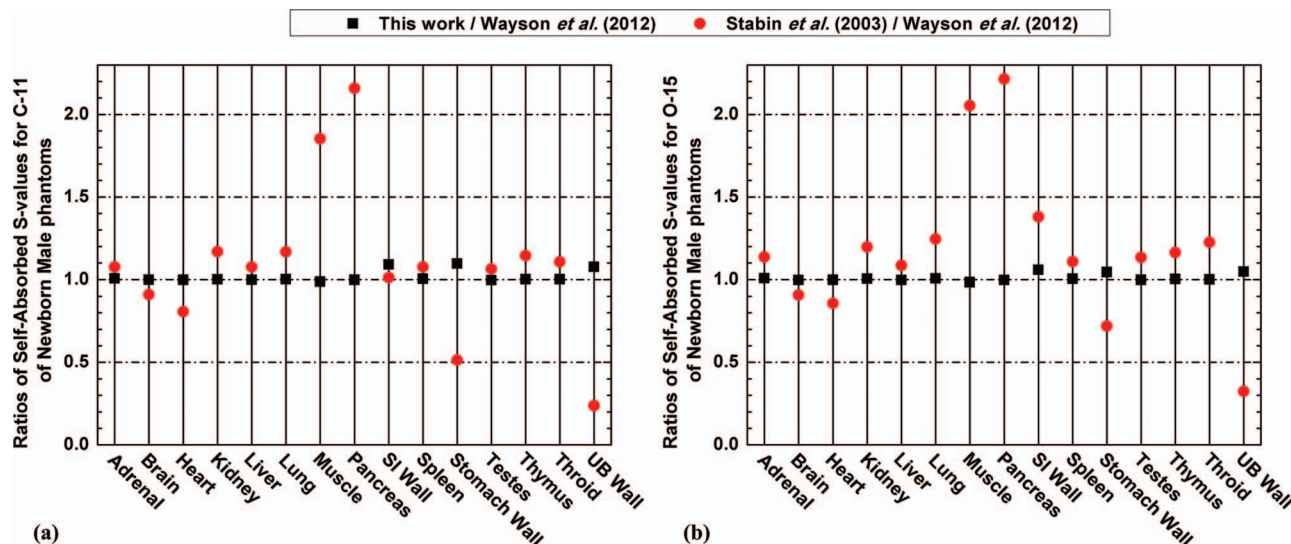


FIG. 6. Ratios between self-absorbed S-values of the newborn male phantom obtained in this work and reported by Stabin and Siegel (Ref. 53) to those reported by Wayson *et al.* (Ref. 46) for (a) C-11 and (b) O-15.

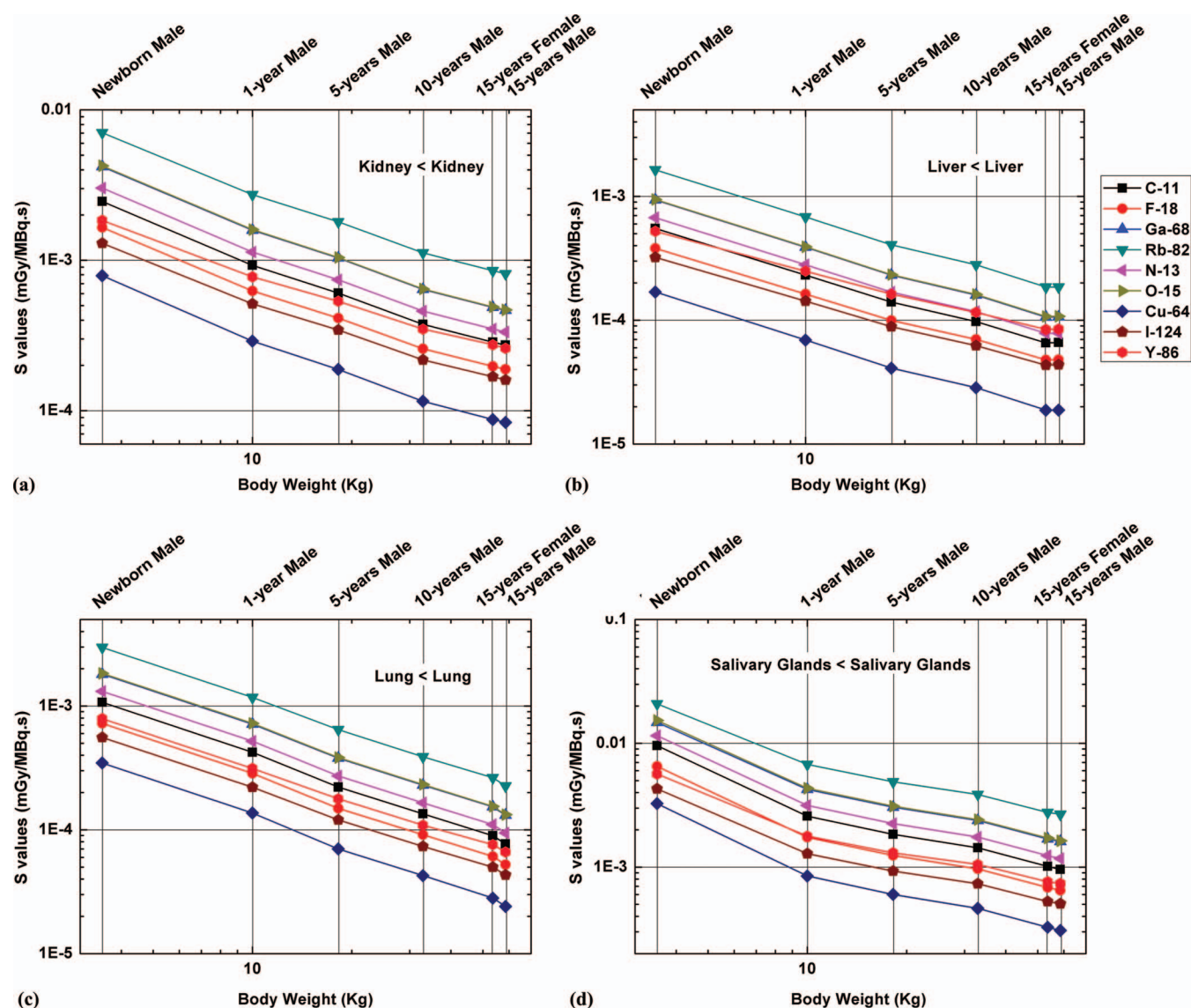


FIG. 7. Self-absorbed  $S$ -values for the (a) kidney, (b) liver, (c) lung, and (d) salivary glands of various pediatric phantoms for the considered positron-emitting radionuclides.

of organs decrease when the body weight increases. The correlation between cross-absorbed  $S$ -values and body weight is more complicated because the energy deposited by particles in the target region from cross-irradiation is more affected by source/target distance. Rb-82 produces the largest self-absorbed  $S$ -values for most organs. The self-absorbed organ  $S$ -values for O-15 and Ga-68 are quite similar and about 42% smaller than those obtained for Rb-82. For most source-target organ pairs, the largest cross-absorbed  $S$ -values are obtained for Y-86. Cu-64 produces the smallest self-absorbed and cross-absorbed  $S$ -values in each source/target organ pair because it emits Auger electrons of low energy (0.8 keV) with height frequency (57%). Figure 9 shows the  $S$ -values of the total body irradiating selected target regions in male and female pediatric phantoms for the 9 considered positron-emitting radionuclides. For most organs, the  $S$ -values of total body irradiation scenarios are close to the total body self-absorbed

$S$ -value, whereas for the lung, the  $S$ -values are about 110% higher than total body self-absorbed  $S$ -value.

### 3.C. Relative contributions of particles to absorbed dose

Figure 10 shows the relative contributions of electrons, positrons, the two annihilation photons and other photons to  $S$ -values of the liver irradiating the liver and adrenal from different positron-emitting radionuclides. It can be seen that for some radionuclides (C-11, F-18, Ga-68, Rb-82, N-13, and O-15), the larger contribution (more than 70%) to the self-absorbed  $S$ -values is due to positron interactions. For the cross-absorbed  $S$ -values of C-11, F-18, Ga-68, N-13, O-15, and Cu-64, more than 80% of the total dose is contributed by the 511 keV annihilation photons. In the MIRD Pamphlet No. 11, the self-absorbed  $S$ -value from photons

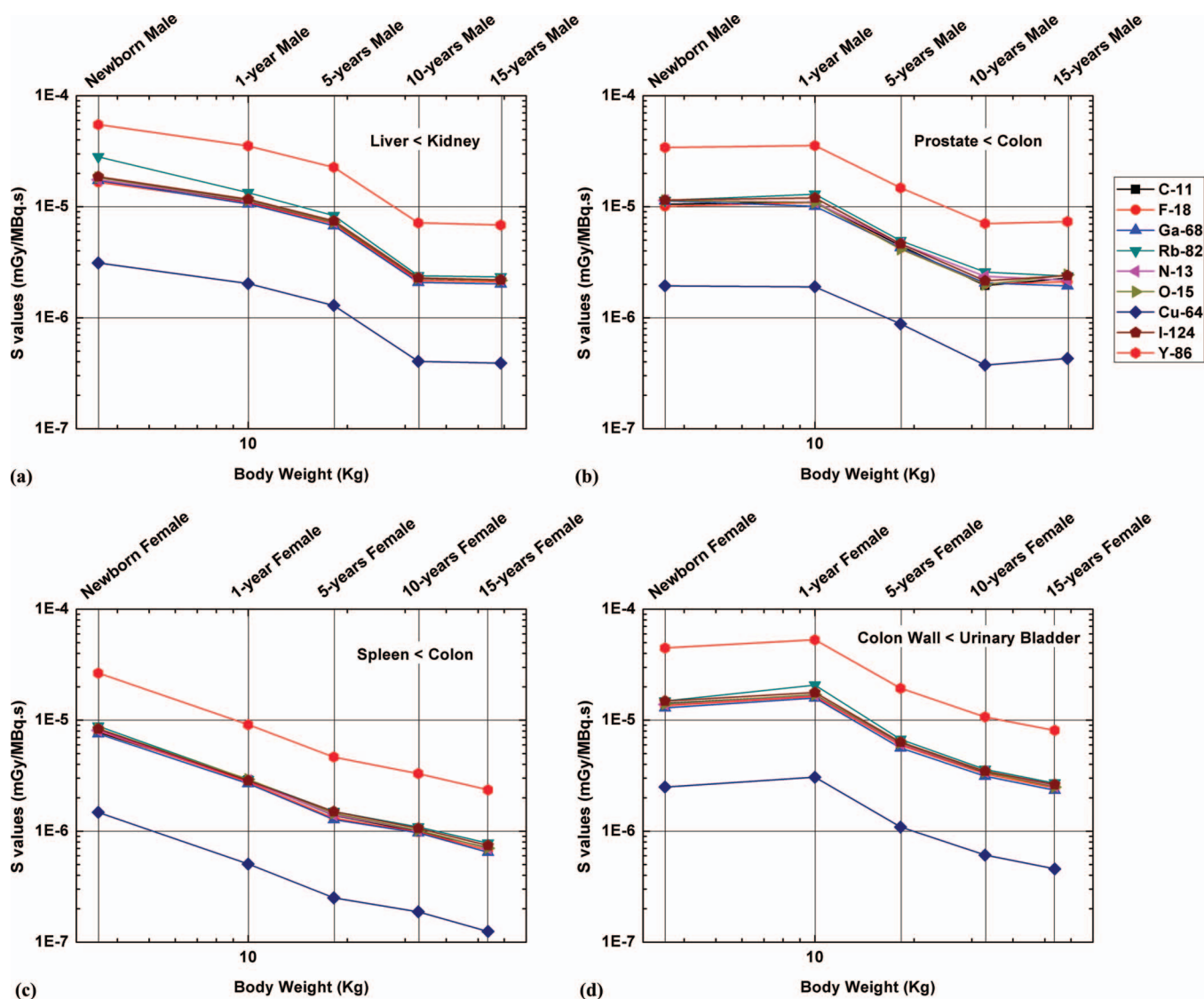


FIG. 8. Cross-absorbed  $S$ -values for (a) the kidney irradiating the liver and (b) the colon irradiating the prostate for the pediatric male phantoms, and (c) the colon irradiating the spleen and (d) the urinary bladder irradiating the colon wall in the female pediatric phantoms.

with energies above 100 keV is considered to be proportional to the organ mass raised to the  $2/3$  power.<sup>52</sup> Some investigators argue that this rule is reasonably accurate for calculation of patient-dependent  $S$ -values from the reported phantom self-absorbed  $S$ -values using the linear mass scaling method.<sup>54,55</sup> In this work, we evaluated the relationship between body weight and total body  $S$ -values for various decay schemes of positron-emitters. Figure 11 compares the contributions of different types of radiation emitted by Ga-68 and I-124 to the total body self-absorbed  $S$ -values between different pediatric male phantoms. It can be observed that when the weight and age of phantoms increase, the contribution of photons and positrons increases and decreases, respectively. The dependence of total body self-absorbed  $S$ -value on body weight for different types of radiation emitted by the evaluated radionuclides is summarized in Table III.

#### 4. DISCUSSION

PET imaging probes are produced by tagging biological molecules or nanoparticles with positron-emitting radionuclides.<sup>56</sup> C-11 and F-18 are frequently used positron-emitting isotopes in preclinical and clinical research. The former can be easily incorporated into many molecules without significant effect on tracer's biodistribution, whereas the latter is usually employed as a substitute for hydrogen or fluorine in the molecule of interest. Other less commonly used positron emitters include N-13, O-15, Ga-68, Rb-82, Cu-64, Y-86, and I-124.

The Monte Carlo method is a powerful and accurate tool for internal radiation dosimetry calculations where the accurate dose estimate is grounded on reliable computational phantoms that mimic the internal anatomic geometries and physical characteristics of the human body. The equivalent

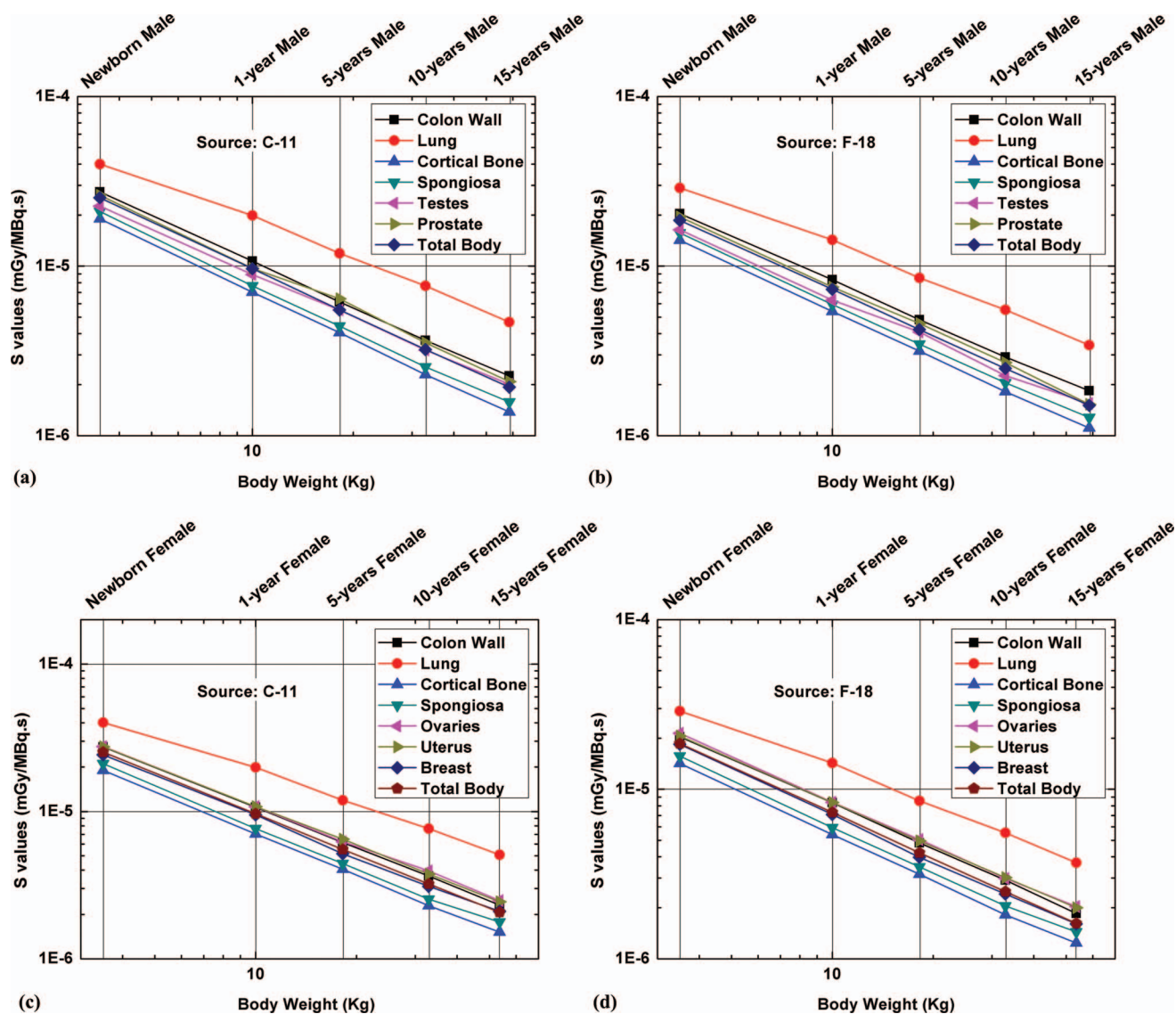


FIG. 9.  $S$ -values of C-11 and F-18 from total body irradiating representative organs of the male pediatric phantoms and the female pediatric phantoms.

radiation dose rate of positron-emitting radionuclides for the pediatric population is frequently calculated from tabulated absorbed fractions of monoenergetic particles derived from mathematical phantoms.<sup>23,24,41–43,53</sup> However, significant differences between the dosimetric characteristics of stylized and voxel-based models for the same subject are often reported.<sup>44–47</sup> In the case of the newborn, the variations of the estimated self-absorbed  $S$ -values for positron-emitting radionuclides may range from  $-78\%$  to  $132\%$  between stylized and voxel-based phantoms in representative organs. Since some biological tissues in children may have substantially different physical characteristics and tissue chemical compositions and present with significantly different radiosensitivity and bioavailability for various radiotracers at different ages, the evaluation of age-dependent absorbed dose using realistic anatomical anthropomorphic pediatric phantoms is commended.

In this work, we calculated the AFs and SAFs of monoenergetic photons and electrons and the  $S$ -values of commonly used positron-emitting radionuclides for reference pe-

diatric phantoms developed at the University of Florida and the National Cancer Institute.<sup>36,37</sup> In these 10 computational phantoms, the photon and electron self AFs present a negative correlation with particle energy and a positive correlation with body weight. This can be explained by the fact that increasing energy facilitates the escape of particles from the source region, and the increased weight is accompanied by bigger volume which expands the distance of particle transport, thus causing more energy deposition in the source organ. The self-absorbed SAFs present an inverse correlation with body weight and source energy. Ionizing radiation may result in significantly higher absorbed dose in the underage children than in the adults.

The variation of  $S$ -values with age and weight was also evaluated for nine commonly used positron-emitting radionuclides in molecular PET imaging. For all organs, the self-absorbed  $S$ -values decrease with increasing age and weight. The cross-absorbed  $S$ -values for different source-target pairs present weak correlation with age and weight. The contribution from positrons, two annihilation photons, electrons, and

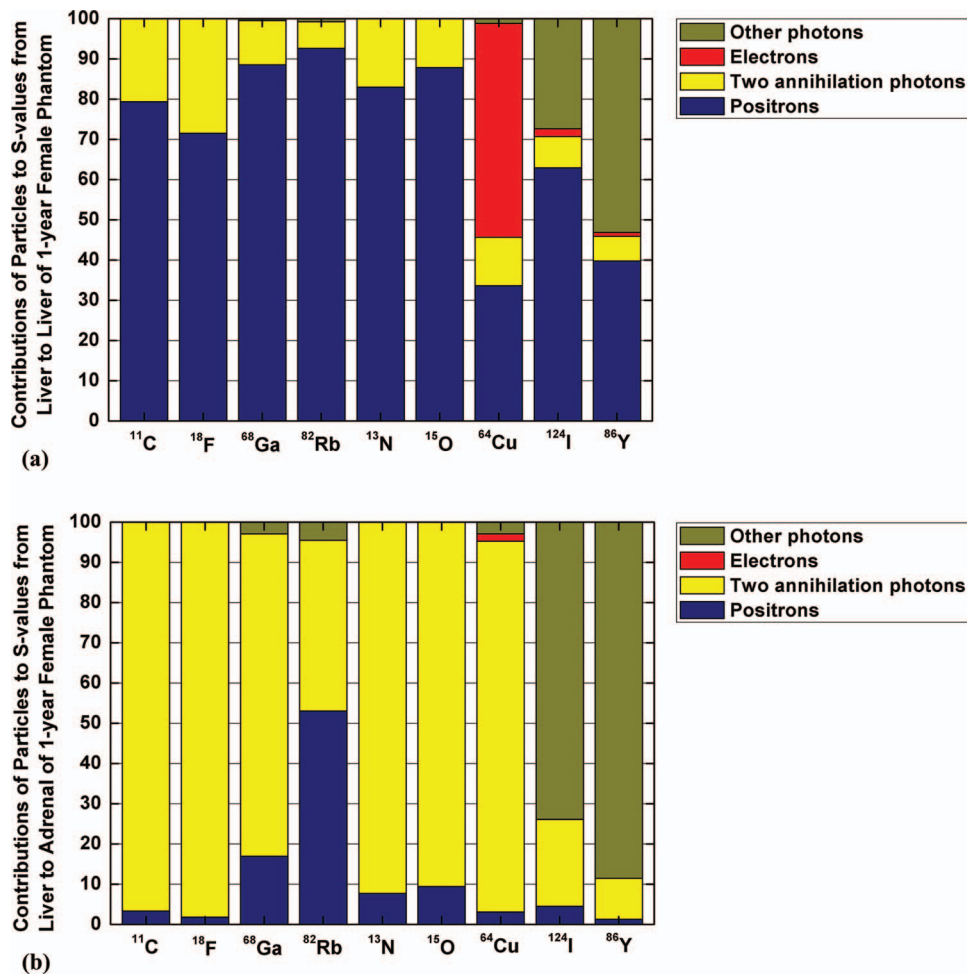


FIG. 10. Relative contributions of different types of radiation (positrons, two annihilation photons, electrons, and other photons) to the estimated  $S$ -values of the liver irradiating (a) the liver and (b) the adrenal of the 1-yr pediatric female phantom.

other photons to the  $S$ -values of organs under self-irradiation and cross-irradiation conditions vary considerably depending on the decay scheme of positron-emitters and body weight. As can be seen in Table III, the dependence of self-absorbed  $S$ -values of the two annihilation photons varies to the reciprocal of 0.76 power of the mass, whereas the self-absorbed  $S$ -values of positrons vary according to the reciprocal mass. The equations describing the relationship between the total  $S$ -value and the mass in Table III demonstrate that linear mass scaling is not appropriate for  $S$ -values of positron-emitters. Since more than 99.9% of the absorbed dose from some radionuclides (C-11, F-18, N-13, and O-15) is contributed by positrons and the two annihilation photons, the total body self-absorbed  $S$ -values for these radionuclides can be calculated as

$$S_{\text{total}}(TB \leftarrow TB) = S_{\text{two annihilation photons}} + S_{\text{positrons}}. \quad (6)$$

Considering Eq. (5) and the dependence of  $S$ -values mainly on positrons and the two annihilation photons (Table III), Eq. (6) can be approximated as follows for some radionuclides (C-11, F-18, N-13, and O-15):

$$S_{\text{total}}(TB \leftarrow TB) = 0.16 \times Y_i \times [0.0235 \times \text{mass}^{-0.76} + E_i \times \text{mass}^{-1}], \quad (7)$$

where 0.16 is a coefficient for unit transformation, 0.0235 and  $-0.76$  are fitting parameters correlated with energy absorption of 511 keV photons in the body, and  $Y_i$  and  $E_i$  are the yield and energy of positron emission. The error between Eq. (7) and the simulated total body self-absorbed  $S$ -values over the newborn to 15-yr children mass range are  $-1.2\%$ – $1.4\%$  for C-11,  $-2.1\%$ – $1.4\%$  for F-18,  $-0.7\%$ – $1.5\%$  for N-13, and  $0.5\%$ – $2.1\%$  for O-15. This nonlinear rule is more suitable for mass scaling to calculate patient-specified total body absorbed dose of C-11, F-18, N-13, and O-15 labeled tracers.

The uncertainty associated with the calculation of organ absorbed dose depends on the uncertainties in the cumulated activity and the  $S$ -value. The variations in the quantitative description of tracer uptake, distribution, and retention of the radiopharmaceutical in organs/tissues can introduce considerable uncertainty in the estimated cumulated activity.<sup>43,57,58</sup> The source geometry may also affect the calculation of  $S$ -values. The assumption of uniformly distributed sources used in this work is consistent with hypotheses followed in the literature<sup>20,46,53</sup> and is traditionally considered sufficient for risk estimation in diagnostic procedures.<sup>59</sup> The application of phantom-dependent parameters of SAF and  $S$ -values to individuals may introduce relatively low uncertainties (about tens of percentage points), and these uncertainties are mainly

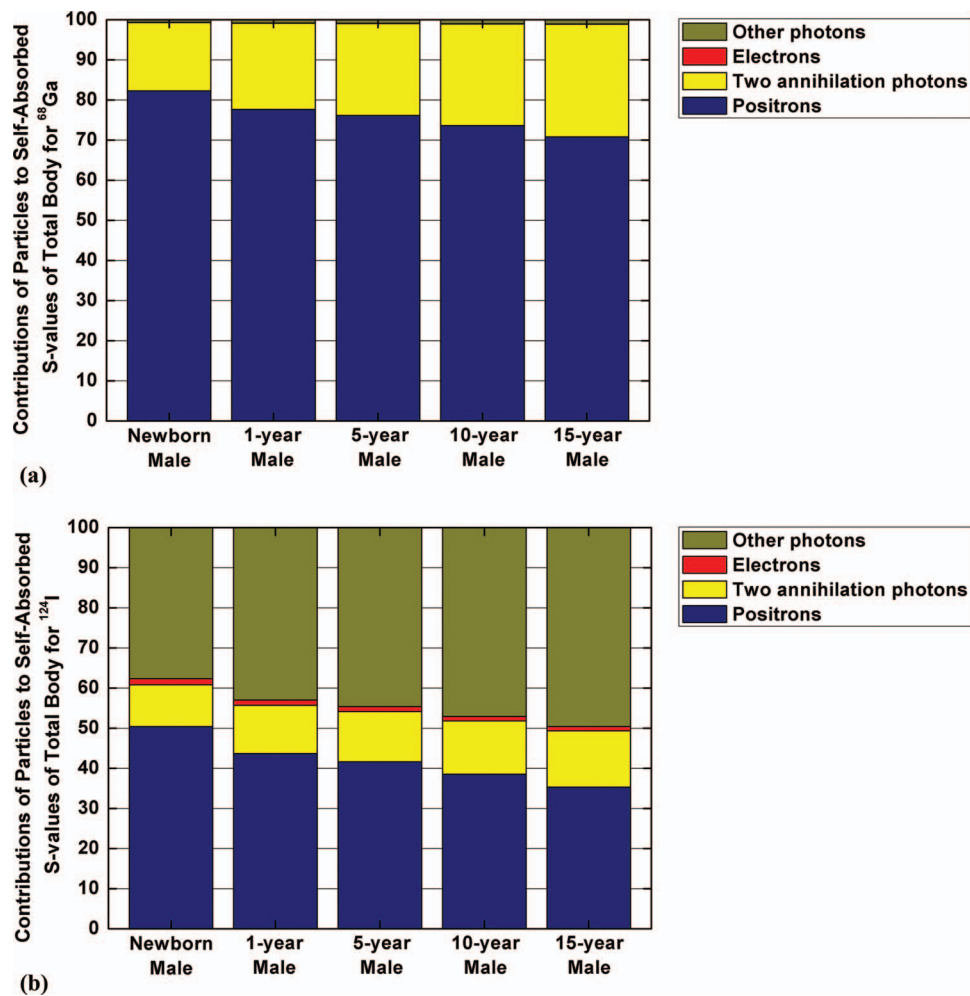


FIG. 11. Relative contributions of different types of radiation (positrons, two annihilation photons, electrons, and other photons) to the estimated self-absorbed  $S$ -values of the total body for the five pediatric male phantoms for (a) Ga-68 and (b) I-124.

contributed by the variation in anatomic aspects, such as the mass of the target organ and the source-target distance. It has already been reported that changes in the adult body size produce differences between 0.3% and 1.1%/kg in SAFs for organs within the trunk.<sup>60</sup> The effect of obesity on dose calculations for internal emitters is reported to be minor and was considered negligible in the routine use of standardized dose estimates.<sup>61</sup> Comparable results were also reported more recently using small-animal models.<sup>62</sup> Therefore, similar ef-

fects of body habitus on internal dosimetry may also be expected for pediatric phantoms. The application of phantom-dependent parameters of SAF and  $S$ -values to individuals may introduce relatively low uncertainties (about tens of percentage points), and these uncertainties are mainly contributed by the variation in anatomic aspects, such as the mass of the target organ and the source-target distance. Meanwhile, the uncertainties associated with biokinetic parameters are at least a factor of 2, because of the variation of tracer uptake,

TABLE III. Total body self-absorbed  $S$ -values (mGy/MBq.s) dependence on different types of radiation for the considered positron-emitting radionuclides.

Isotopes	$S_{\text{other photons}}$	$S_{\text{electrons}}$	$S_{\text{two annihilation photons}}$	$S_{\text{positrons}}$	Total $S$ -value
$^{11}\text{C}$	-	-	$(3.82 \times 10^{-3}) \times \text{mass}^{-0.76}$	$(5.89 \times 10^{-2}) \times \text{mass}^{-1.00}$	$(4.28 \times 10^{-2}) \times \text{mass}^{-0.91}$
$^{18}\text{F}$	-	-	$(3.70 \times 10^{-3}) \times \text{mass}^{-0.76}$	$(3.88 \times 10^{-2}) \times \text{mass}^{-1.00}$	$(2.58 \times 10^{-2}) \times \text{mass}^{-0.89}$
$^{68}\text{Ga}$	$(1.42 \times 10^{-4}) \times \text{mass}^{-0.77}$	$(8.35 \times 10^{-5}) \times \text{mass}^{-1.00}$	$(3.22 \times 10^{-3}) \times \text{mass}^{-0.75}$	$(1.09 \times 10^{-1}) \times \text{mass}^{-0.99}$	$(8.88 \times 10^{-2}) \times \text{mass}^{-0.94}$
$^{82}\text{Rb}$	$(4.28 \times 10^{-4}) \times \text{mass}^{-0.76}$	$(4.82 \times 10^{-5}) \times \text{mass}^{-1.00}$	$(3.22 \times 10^{-3}) \times \text{mass}^{-0.75}$	$(1.95 \times 10^{-1}) \times \text{mass}^{-0.99}$	$(1.69 \times 10^{-1}) \times \text{mass}^{-0.96}$
$^{13}\text{N}$	-	-	$(3.75 \times 10^{-3}) \times \text{mass}^{-0.76}$	$(7.54 \times 10^{-2}) \times \text{mass}^{-1.00}$	$(5.57 \times 10^{-2}) \times \text{mass}^{-0.92}$
$^{15}\text{O}$	-	-	$(3.64 \times 10^{-3}) \times \text{mass}^{-0.76}$	$(1.08 \times 10^{-1}) \times \text{mass}^{-0.99}$	$(8.72 \times 10^{-2}) \times \text{mass}^{-0.94}$
$^{64}\text{Cu}$	$(1.25 \times 10^{-4}) \times \text{mass}^{-0.88}$	$(1.20 \times 10^{-2}) \times \text{mass}^{-1.00}$	$(6.69 \times 10^{-4}) \times \text{mass}^{-0.76}$	$(7.49 \times 10^{-3}) \times \text{mass}^{-1.00}$	$(1.56 \times 10^{-2}) \times \text{mass}^{-0.94}$
$^{124}\text{I}$	$(3.29 \times 10^{-3}) \times \text{mass}^{-0.76}$	$(8.79 \times 10^{-4}) \times \text{mass}^{-1.00}$	$(8.50 \times 10^{-4}) \times \text{mass}^{-0.76}$	$(2.82 \times 10^{-2}) \times \text{mass}^{-0.99}$	$(2.05 \times 10^{-2}) \times \text{mass}^{-0.87}$
$^{86}\text{Y}$	$(1.05 \times 10^{-2}) \times \text{mass}^{-0.75}$	$(7.70 \times 10^{-4}) \times \text{mass}^{-1.00}$	$(1.18 \times 10^{-3}) \times \text{mass}^{-0.76}$	$(3.18 \times 10^{-2}) \times \text{mass}^{-1.00}$	$(2.61 \times 10^{-2}) \times \text{mass}^{-0.81}$

distribution, and retention of the radiopharmaceutical in tissues of different subjects, particularly in disease states.<sup>63</sup>

## 5. CONCLUSION

A systematic study was performed to evaluate the dosimetric properties of common positron-emitting radionuclides in pediatric phantoms. We also investigated the impact of changes in body weight on the calculation of AFs and SAFs of monoenergetic photons/electrons, and *S*-values of positron-emitting radionuclides. For most organs, the self-AF is positively correlated to the weight, while the SAF and radionuclide-specific *S*-value presents an inverse correlation with body weight. The absorbed dose of different source-target pairs of positron-emitters is mostly contributed by positrons and the two annihilation photons. Since children have higher sensitivity to radiation and smaller body size, the radiation risks associated with clinical PET examinations are a matter of concern. The derived nonlinear mass scaling approach can be used to calculate patient-specific total body absorbed dose of C-11, F-18, N-13, and O-15 labeled tracers. The produced SAFs of monoenergetic photons/electrons and *S*-values of common positron-emitting radionuclides can be exploited to assess the radiation dose delivered by other radionuclides and various radiotracers to the pediatric population.

## ACKNOWLEDGMENTS

This work was supported by the Swiss National Science Foundation under Grant No. SNSF 31003A-135576 and the Geneva Cancer League.

<sup>a)</sup> Author to whom correspondence should be addressed. Electronic mail: habib.zaidi@hcuge.ch; Telephone: +41 22 372 7258; Fax: +41 22 372 7169.

- <sup>1</sup> S. S. Gambhir, "Molecular imaging of cancer with positron emission tomography," *Nat. Rev. Cancer* **2**, 683–693 (2002).
- <sup>2</sup> M. Tatsumi, J. H. Miller, and R. L. Wahl, "18F-FDG PET/CT in evaluating non-CNS pediatric malignancies," *J. Nucl. Med.* **48**, 1923–1931 (2007).
- <sup>3</sup> H. Jadvar, L. P. Connolly, F. H. Fahey, and B. L. Shulkin, "PET and PET/CT in pediatric oncology," *Semin Nucl. Med.* **37**, 316–331 (2007).
- <sup>4</sup> M. Kleis, H. Daldrup-Link, K. Matthay, R. Goldsby, Y. Lu, T. Schuster, C. Schreck, P. W. Chu, R. A. Hawkins, and B. L. Franc, "Diagnostic value of PET/CT for the staging and restaging of pediatric tumors," *Eur. J. Nucl. Med. Mol. Imaging* **36**, 23–36 (2009).
- <sup>5</sup> A. M. Alessio, P. E. Kinahan, V. Manchanda, V. Ghioni, L. Aldape, and M. T. Parisi, "Weight-based, low-dose pediatric whole-body PET/CT protocols," *J. Nucl. Med.* **50**, 1570–1578 (2009).
- <sup>6</sup> R. Accorsi, J. S. Karp, and S. Surti, "Improved dose regimen in pediatric PET," *J. Nucl. Med.* **51**, 293–300 (2010).
- <sup>7</sup> S. C. Chawla, N. Federman, D. Zhang, K. Nagata, S. Nuthakki, M. McNitt-Gray, and M. I. Boechat, "Estimated cumulative radiation dose from PET/CT in children with malignancies: A 5-year retrospective review," *Pediatr. Radiol.* **40**, 681–686 (2010).
- <sup>8</sup> F. H. Fahey, S. T. Treves, and S. J. Adelstein, "Minimizing and communicating radiation risk in pediatric nuclear medicine," *J. Nucl. Med.* **52**, 1240–1251 (2011).
- <sup>9</sup> S. T. Treves, M. T. Parisi, and M. J. Gelfand, "Pediatric radiopharmaceutical doses: New guidelines," *Radiology* **261**, 347–349 (2011).
- <sup>10</sup> E. Robbins, "Radiation risks from imaging studies in children with cancer," *Pediatr. Blood Cancer* **51**, 453–457 (2008).

- <sup>11</sup> K. N. Prasad, W. C. Cole, and G. M. Hasse, "Health risks of low dose ionizing radiation in humans: A review," *Exp. Biol. Med.* **229**, 378–382 (2004).
- <sup>12</sup> C. Mothersill and C. Seymour, "Implications for human and environmental health of low doses of ionising radiation," *J. Environ. Radioact.* (in press).
- <sup>13</sup> M. S. Parker, F. K. Hui, M. A. Camacho, J. K. Chung, D. W. Broga, and N. N. Sethi, "Female breast radiation exposure during CT pulmonary angiography," *AJR, Am. J. Roentgenol.* **185**, 1228–1233 (2005).
- <sup>14</sup> M. Steinert, M. Weiss, P. Gottlober, D. Belyi, O. Gergel, V. Bebesko, N. Nadejina, I. Galstian, G. Wagemaker, T. M. Fliedner, and R. U. Peter, "Delayed effects of accidental cutaneous radiation exposure: Fifteen years of follow-up after the Chernobyl accident," *J. Am. Acad. Dermatol.* **49**, 417–423 (2003).
- <sup>15</sup> H. Zaidi and X. G. Xu, "Computational anthropomorphic models of the human anatomy: The path to realistic Monte Carlo modeling in medical imaging," *Annu. Rev. Biomed. Eng.* **9**, 471–500 (2007).
- <sup>16</sup> H. Fisher, Jr. and W. Snyder, "Variation of dose delivered by <sup>137</sup>Cs as a function of body size from infancy to adulthood," *ORNL* **4007**, 221–228 (1966).
- <sup>17</sup> M. Cristy, "Mathematical phantoms representing children of various ages for use in estimates of internal dose" (Oak Ridge National Lab., TN, 1980).
- <sup>18</sup> E. Y. Han, W. E. Bolch, and K. F. Eckerman, "Revisions to the ORNL series of adult and pediatric computational phantoms for use with the MIRD schema," *Health Phys.* **90**, 337–356 (2006).
- <sup>19</sup> X. G. Xu and K. F. Eckerman, *Handbook of Anatomical Models for Radiation Dosimetry* (CRC Press/Taylor and Francis, Boca Raton, FL, 2009), pp. 576.
- <sup>20</sup> W. S. Snyder, M. R. Ford, and G. G. Warner, *MIRD Pamphlet No. 5 (Revised): Estimates of Absorbed Fractions for Monoenergetic Photon Sources Uniformly Distributed in Various Organs of a Heterogeneous Phantom* (The Society of Nuclear Medicine, New York, 1978).
- <sup>21</sup> R. Loevinger, T. F. Budinger, and E. E. Watson, *MIRD Primer for Absorbed Dose Calculations, Revised* (The Society of Nuclear Medicine, New York, 1991).
- <sup>22</sup> L. G. Bouchet, W. E. Bolch, D. A. Weber, H. L. Atkins, and J. W. Poston, "MIRD Pamphlet No. 15: Radionuclide S values in a revised dosimetric model of the adult head and brain. Medical Internal Radiation Dose," *J. Nucl. Med.* **40**, 62S–101S (1999).
- <sup>23</sup> M. G. Stabin, "MIRDose: Personal computer software for internal dose assessment in nuclear medicine," *J. Nucl. Med.* **37**, 538–546 (1996).
- <sup>24</sup> M. G. Stabin, R. B. Sparks, and E. Crowe, "OLINDA/EXM: The second-generation personal computer software for internal dose assessment in nuclear medicine," *J. Nucl. Med.* **46**, 1023–1027 (2005).
- <sup>25</sup> G. Williams, M. Zankl, W. Abmayr, R. Veit, and G. Drexler, "The calculation of dose from external photon exposures using reference and realistic human phantoms and Monte Carlo methods," *Phys. Med. Biol.* **31**, 449–452 (1986).
- <sup>26</sup> M. Zankl, R. Veit, G. Williams, K. Schneider, H. Fendel, N. Petoussi, and G. Drexler, "The construction of computer tomographic phantoms and their application in radiology and radiation protection," *Radiat. Environ. Biophys.* **27**, 153–164 (1988).
- <sup>27</sup> N. Petoussi-Hens, M. Zankl, U. Fill, and D. Regulla, "The GSF family of voxel phantoms," *Phys. Med. Biol.* **47**, 89–106 (2002).
- <sup>28</sup> A. Christ, W. Kainz, E. G. Hahn, K. Honegger, M. Zefferer, E. Neufeld, W. Rascher, R. Janka, W. Bautz, J. Chen, B. Kiefer, P. Schmitt, H.-P. Hollenbach, J. Shen, M. Oberle, D. Szczerba, A. Kam, J. W. Guag, and N. Kuster, "The virtual family-development of surface-based anatomical models of two adults and two children for dosimetric simulations," *Phys. Med. Biol.* **55**, N23–N38 (2010).
- <sup>29</sup> T. Nagaoka, E. Kunieda, and S. Watanabe, "Proportion-corrected scaled voxel models for Japanese children and their application to the numerical dosimetry of specific absorption rate for frequencies from 30 MHz to 3 GHz," *Phys. Med. Biol.* **53**, 6695–6711 (2008).
- <sup>30</sup> X. Li, E. Samei, W. P. Segars, G. M. Sturgeon, J. G. Colsher, G. Toncheva, T. T. Yoshizumi, and D. P. Frush, "Patient-specific radiation dose and cancer risk estimation in CT: Part I. Development and validation of a Monte Carlo program," *Med. Phys.* **38**, 397–407 (2011).
- <sup>31</sup> J. C. Nipper, J. L. Williams, and W. E. Bolch, "Creation of two tomographic voxel models of pediatric patients in the first year of life," *Phys. Med. Biol.* **47**, 3143–3164 (2002).
- <sup>32</sup> C. Lee, J. L. Williams, and W. E. Bolch, "Whole-body voxel phantoms of pediatric patients—UF Series B," *Phys. Med. Biol.* **51**, 4649–4661 (2006).

- <sup>33</sup>C. Lee, J. L. Williams, C. Lee, and W. Bolch, "The UF series of tomographic computational phantoms of pediatric patients," *Med. Phys.* **32**, 3537–3548 (2005).
- <sup>34</sup>W. P. Segars, J. Bond, J. Frush, S. Hon, C. Eckersley, C. H. Williams, J. Feng, D. J. Tward, J. T. Ratnanather, M. I. Miller, D. Frush, and E. Samei, "Population of anatomically variable 4D XCAT adult phantoms for imaging research and optimization," *Med. Phys.* **40**, 043701 (11pp.) (2013).
- <sup>35</sup>ICRP, "Basic anatomical and physiological data for use in radiological protection: Reference values: ICRP Publication 89," *Ann. ICRP* **32**, 1–277 (2002).
- <sup>36</sup>C. Lee, D. Lodwick, D. Hasenauer, J. L. Williams, and W. E. Bolch, "Hybrid computational phantoms of the male and female newborn patient: NURBS-based whole-body models," *Phys. Med. Biol.* **52**, 3309–3333 (2007).
- <sup>37</sup>C. Lee, D. Lodwick, J. Hurtado, D. Pafundi, J. L. Williams, and W. E. Bolch, "The UF family of reference hybrid phantoms for computational radiation dosimetry," *Phys. Med. Biol.* **55**, 339–363 (2010).
- <sup>38</sup>V. J. Lima, V. F. Cassola, R. Kramer, C. A. Lira, H. J. Khoury, and J. W. Vieira, "Development of 5- and 10-year-old pediatric phantoms based on polygon mesh surfaces," *Med. Phys.* **38**, 4723–4736 (2011).
- <sup>39</sup>M. G. Stabin, X. G. Xu, M. A. Emmons, W. P. Segars, C. Shi, and M. J. Fernald, "RADAR reference adult, pediatric, and pregnant female phantom series for internal and external dosimetry," *J. Nucl. Med.* **53**, 1807–1813 (2012).
- <sup>40</sup>U. Eberlein, J. H. Broer, C. Vandevoorde, P. Santos, M. Bardies, K. Bacher, D. Nosske, and M. Lassmann, "Biokinetics and dosimetry of commonly used radiopharmaceuticals in diagnostic nuclear medicine - A review," *Eur. J. Nucl. Med. Mol. Imaging* **38**, 2269–2281 (2011).
- <sup>41</sup>ICRP, "ICRP Publication 53: Radiation dose to patients from radiopharmaceuticals," *Ann. ICRP* **18**, 1–377 (1987).
- <sup>42</sup>ICRP, "ICRP publication 80: Radiation dose to patients from radiopharmaceuticals (addendum 2 to ICRP publication 53)," *Ann. ICRP* **28**, 1–126 (1998).
- <sup>43</sup>ICRP, "ICRP Publication 106: Radiation dose to patients from radiopharmaceuticals. Addendum 3 to ICRP Publication 53," *Ann. ICRP* **38**, 1–197 (2008).
- <sup>44</sup>R. Kramer, H. J. Khoury, and J. W. Vieira, "Comparison between effective doses for voxel-based and stylized exposure models from photon and electron irradiation," *Phys. Med. Biol.* **21**, 5105–5126 (2005).
- <sup>45</sup>T. Xie, G. Zhang, Y. Li, and Q. Liu, "Comparison of absorbed fractions of electrons and photons using three kinds of computational phantoms of rat," *Appl. Phys. Lett.* **97**, 033702–033704 (2010).
- <sup>46</sup>M. Wayson, C. Lee, G. Sgouros, S. T. Treves, E. Frey, and W. E. Bolch, "Internal photon and electron dosimetry of the newborn patient—a hybrid computational phantom study," *Phys. Med. Biol.* **57**, 1433–1457 (2012).
- <sup>47</sup>T. Xie and H. Zaidi, "Assessment of S-values in stylized and voxel-based rat models for positron-emitting radionuclides," *Mol. Imaging Biol.* (in press).
- <sup>48</sup>ICRP, "ICRP Publication 103: The 2007 Recommendations of the International Commission on Radiological Protection," *Ann. ICRP* **37**, 1–332 (2007).
- <sup>49</sup>D. Pelowitz, "MCNPX Version 2.5.0 User's Manual" (Los Alamos National Laboratory, Los Alamos, NM, 2005).
- <sup>50</sup>HPS, "<http://hps.org/publicinformation/radardecaydata.cfm>," (2012).
- <sup>51</sup>W. E. Bolch, K. F. Eckerman, G. Sgouros, and S. R. Thomas, "MIRD Pamphlet No. 21: A generalized schema for radiopharmaceutical dosimetry - Standardization of nomenclature," *J. Nucl. Med.* **50**, 477–484 (2009).
- <sup>52</sup>W. S. Snyder, M. R. Ford, G. G. Warner, and S. B. Watson, *MIRD Pamphlet No. 11: 'S', Absorbed Dose Per Unit Cumulated Activity for Selected Radionuclides and Organs* (The Society of Nuclear Medicine, New York, 1975).
- <sup>53</sup>M. G. Stabin and J. A. Siegel, "Physical models and dose factors for use in internal dose assessment," *Health Phys.* **85**, 294–310 (2003).
- <sup>54</sup>A. C. Traino, M. Ferrari, M. Cremonesi, and M. G. Stabin, "Influence of total-body mass on the scaling of S-factors for patient-specific, blood-based red-marrow dosimetry," *Phys. Med. Biol.* **52**, 5231–5248 (2007).
- <sup>55</sup>J. A. Siegel and M. G. Stabin, "Mass scaling of S values for blood-based estimation of red marrow absorbed dose: The quest for an appropriate method," *J. Nucl. Med.* **48**, 253–256 (2007).
- <sup>56</sup>J. F. Valliant, "A bridge not too far: Linking disciplines through molecular imaging probes," *J. Nucl. Med.* **51**, 1258–1268 (2010).
- <sup>57</sup>K. Norrgren, S. L. Svegborn, J. Areberg, and S. Mattsson, "Accuracy of the quantification of organ activity from planar gamma camera images," *Cancer Biother. Radiopharm.* **18**, 125–131 (2003).
- <sup>58</sup>L. Jönsson, M. Ljungberg, and S.-E. Strand, "Evaluation of accuracy in activity calculations for the conjugate view method from Monte Carlo simulated scintillation camera images using experimental data in an anthropomorphic phantom," *J. Nucl. Med.* **46**, 1679–1686 (2005).
- <sup>59</sup>W. Bolch, L. Bouchet, J. Robertson, B. Wessels, J. Siegel, R. Howell, A. Erdi, B. Aydogan, S. Costes, and E. Watson, "MIRD pamphlet No. 17: The dosimetry of nonuniform activity distributions—radionuclide S values at the voxel level. Medical Internal Radiation Dose Committee," *J. Nucl. Med.* **40**, 11S–36S (1999).
- <sup>60</sup>P. M. Marine, M. G. Stabin, M. J. Fernald, and A. B. Brill, "Changes in radiation dose with variations in human anatomy: Larger and smaller normal-stature adults," *J. Nucl. Med.* **51**, 806–811 (2010).
- <sup>61</sup>L. D. Clark, M. G. Stabin, M. J. Fernald, and A. B. Brill, "Changes in radiation dose with variations in human anatomy: Moderately and severely obese adults," *J. Nucl. Med.* **51**, 929–932 (2010).
- <sup>62</sup>T. Xie and H. Zaidi, "Effect of emaciation and obesity on small animal internal radiation dosimetry for positron-emitting radionuclides," *Eur. J. Nucl. Med. Mol. Imaging* (in press).
- <sup>63</sup>M. G. Stabin, "Uncertainties in internal dose calculations for radiopharmaceuticals," *J. Nucl. Med.* **49**, 853–860 (2008).